

Tectonic modification of axial crustal structure: Evidence from spectral analyses of residual gravity and bathymetry of the Mid-Atlantic Ridge flanks

Javier Escartín^{a,b,*}, Jian Lin^{a,c}

^a Department of Geological Sciences, University of Durham, Durham, DH1 3LE, UK

^b Dept. of Geology and Geophysics, University of Edinburgh, Edinburgh, EH9 3JW, UK

^c Department of Geology and Geophysics, Woods Hole Oceanographic Institution, Woods Hole, MA 02543, USA

Received 6 May 1997; revised 18 September 1997; accepted 25 September 1997

Abstract

Bathymetry and gravity data of the northern Atlantic suggest that oceanic crustal structure on the flanks of the Mid-Atlantic Ridge is strongly modified by tectonic extension at spreading ridge segments. The seafloor along the zero-age isochron is systematically more elevated and the crust thicker near the segment midpoint than at the ends, suggesting focused magmatic accretion at segment centers. In contrast, seafloor older than 2–3 Ma is usually the shallowest at inside corners of ridge-offset intersections, where positive residual gravity anomalies indicate tectonically thinned crust. Coherence between residual gravity and bathymetry for zero-age crust is found at wavelength greater than ~ 20 km, which reflects the characteristic length of ridge segments, and is consistent with an effective elastic plate thickness of 1–3 km. No significant coherence, however, is observed on isochron profiles at ages of 2.5 Ma and older at all wavelengths. Flow-line profiles display coherence at wavelength greater than ~ 5 km, yielding an estimated effective elastic plate thickness of only 0.3–0.5 km. Synthetic fault models suggest that the flow-line coherence may be controlled by the relatively close spacing of fault-generated abyssal hills rather than reflecting the true elastic thickness of unfaulted lithosphere. Together these results indicate that the crustal structure of the zero-age crust is modified strongly by tectonic extension along the rift valley walls of the slow-spreading Mid-Atlantic Ridge. © 1998 Elsevier Science B.V.

Keywords: oceanic crust; extension; mid-ocean ridges; gravity anomalies; crustal thinning

1. Introduction

Morphology, gravity, and seismic data from the slow-spreading Mid-Atlantic Ridge (MAR) reveal that the segmentation of the spreading center strongly controls the oceanic crustal structure. The MAR axis

is divided into segments ~ 20 –100 km in length [1,2]. Within the axial rift valley, the seafloor is systematically shallower and the crust thicker at segment midpoints than at segment ends near both transform and non-transform discontinuities [3–7]. These observations are consistent with models of focused magmatic accretion at the center of segments [4,8,9].

Systematic segment-scale variations in seafloor morphology and crustal thickness are also observed

* Corresponding author. Tel.: +44-131-650-8511; fax: +44-131-668-3184; E-mail: javihu@mail.glg.ed.ac.uk

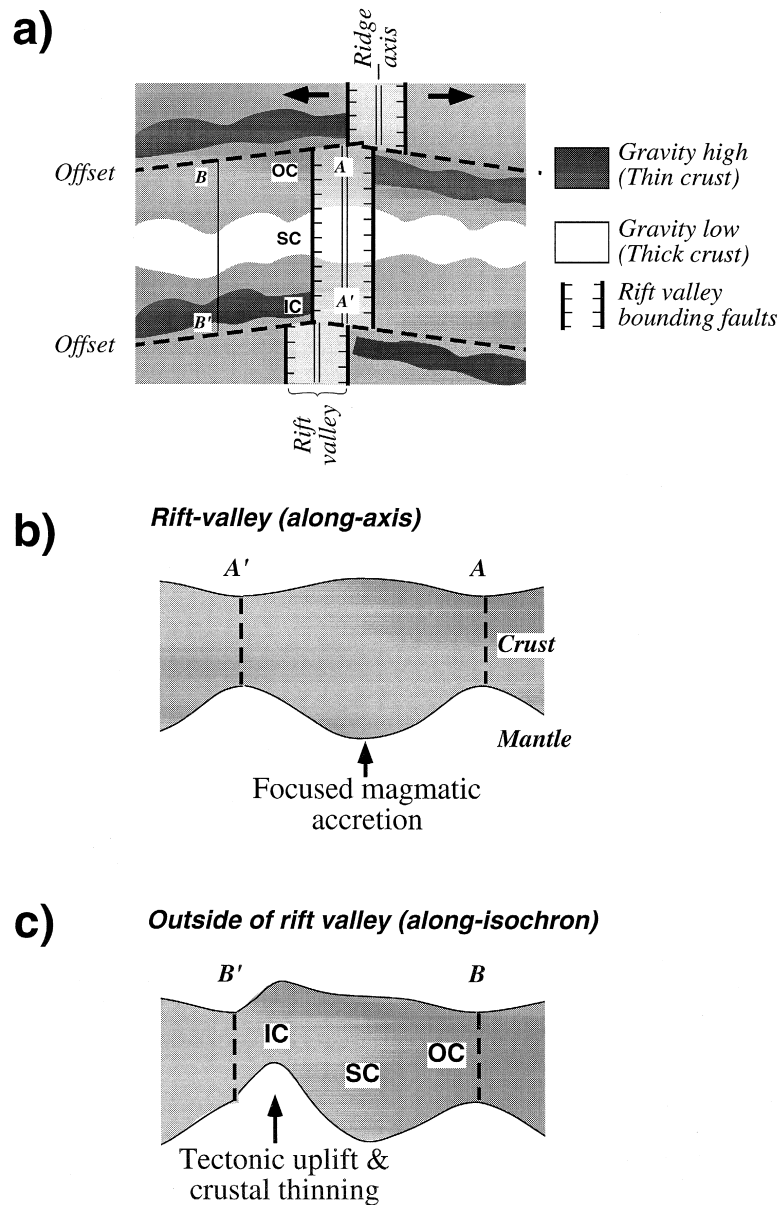


Fig. 1. (a) Sketch of systematic variations in residual gravity structure observed at a segment in the North Atlantic. Typically, residual gravity highs extend along IC crust in the vicinity of segment boundaries and are associated with elevated terrain. In contrast, residual gravity lows tend to be found as ribbons that extend off axis along segment centers.

(b) Typical along-axis depth cross-section of the crust. Focused magmatic accretion at ridge segments may result in elevated topography and thicker crust at segment centers than near their distal ends.

(c) As the crust is rafted off axis, tectonic extension at the rift valley walls may result in tectonic uplift and crustal thinning, particularly at IC crust. Thus tectonic activity along the rift valley may modify the original crustal structure emplaced at the ridge axis, resulting in off-axis ribbons of gravity highs and lows.

off axis, but differ from those on axis. Near discontinuities there is a clear asymmetry in seafloor elevation: inside corners (ICs) are more elevated and have more positive residual gravity anomalies than outside corners (OCs) [10–12]. Data on the MAR flanks reveal off-axis traces of elevated thin IC crust, whereas segment centers (SCs) display relatively thick crust [13–16]. These changes in seafloor mor-

phology and gravity patterns indicate that the off-axis structure of the crust is the product of magmatic accretion at the ridge axis and later tectonic faulting at the rift valley walls. The extent of crustal modification and the processes responsible for it are still poorly understood.

Constraints on tectonic processes that modify the crustal structure can be obtained from the examina-

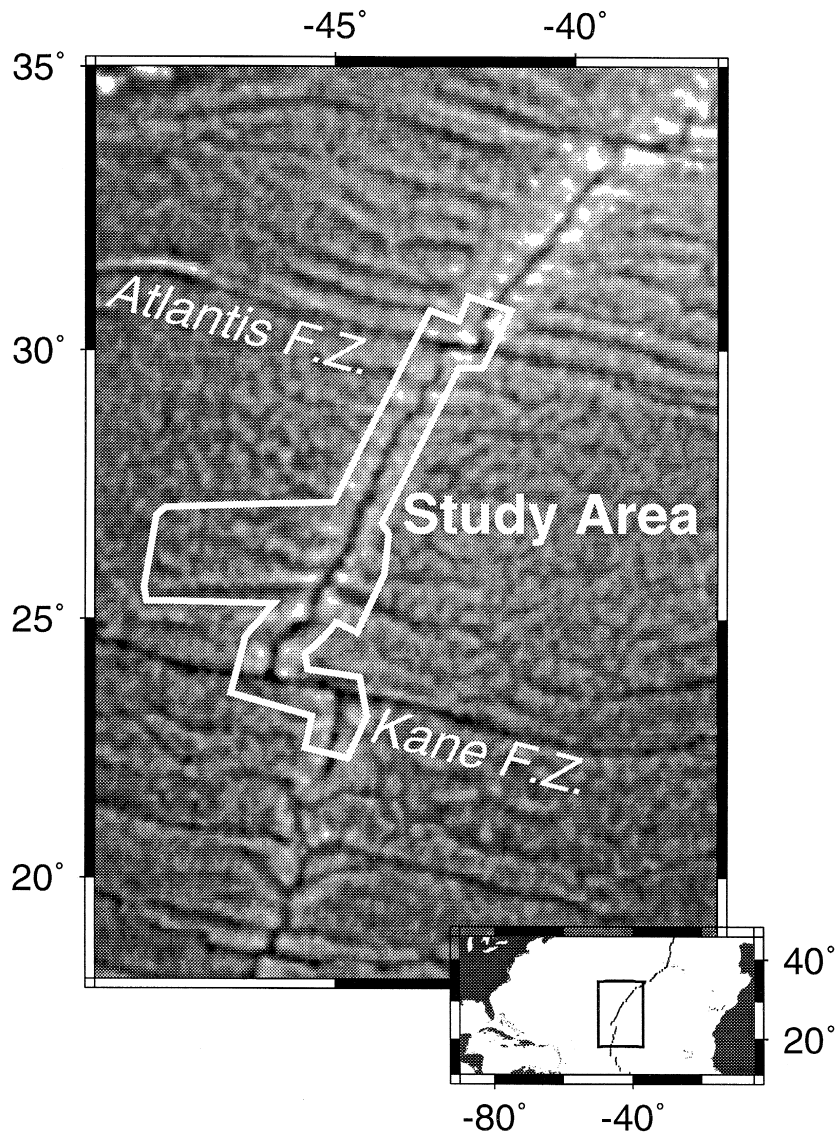


Fig. 2. Location of the study area on the northern Atlantic marked on a free-air gravity anomaly map derived from Geosat and ERS1 satellite altimetry [27]. High-resolution shiptrack data encompasses the ridge axis from south of the Kane FZ to north of the Atlantis FZ, and extends off axis on the western flank between $\sim 25^{\circ}30'$ and $\sim 27^{\circ}10'N$.

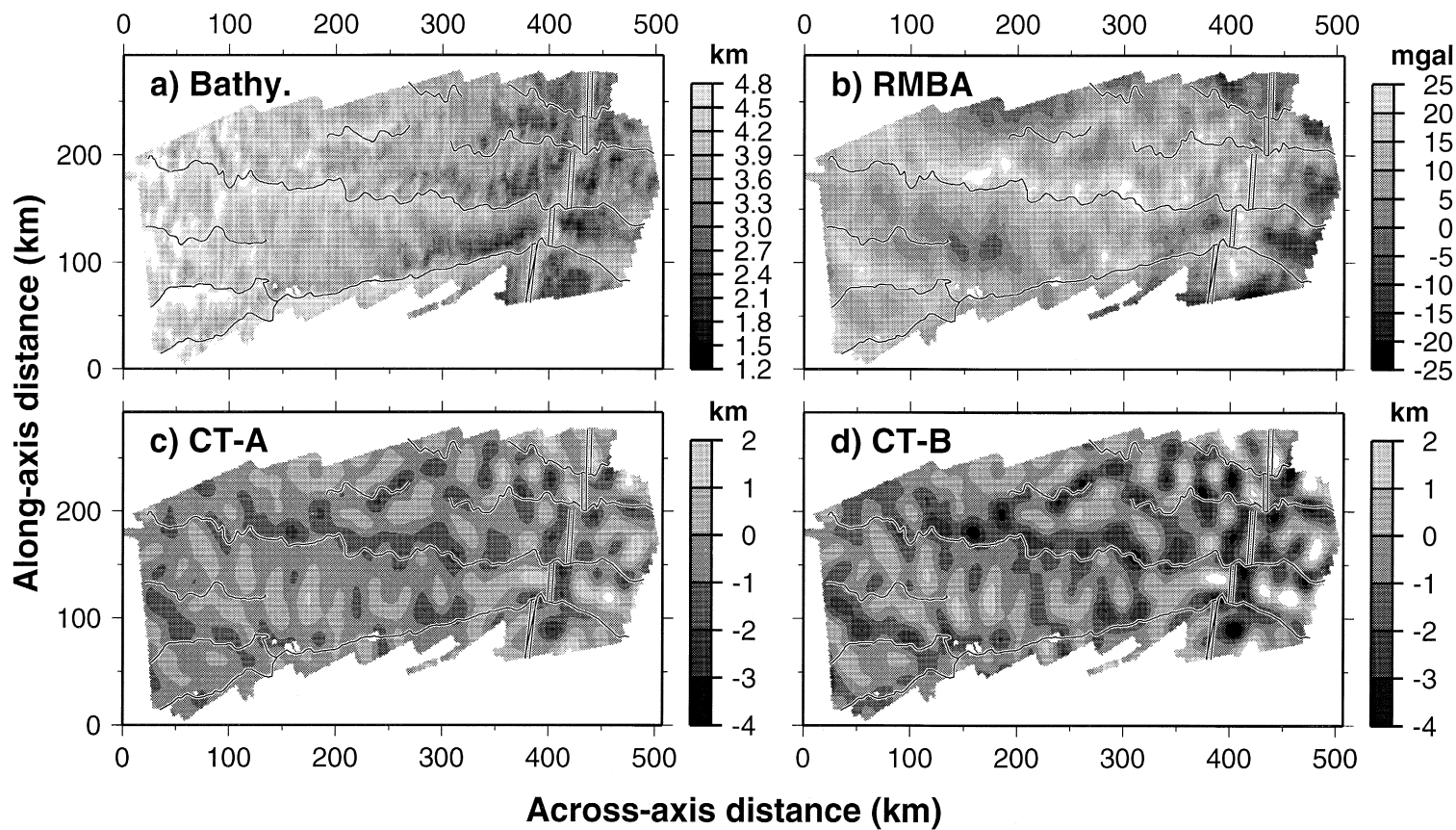


Fig. 3. Rotated grid maps of: (a) bathymetry; (b) residual MBA (RMBA); and (c), (d) maps of relative crustal thickness calculated from the RMBA data for two different crustal density models. (c) Model A corresponds to a single crust layer with constant density of 2700 kg m^{-3} , and (d) model B corresponds to an upper crust of 2 km thick and density of 2600 kg m^{-3} and a lower crust of variable thickness and a density of 2800 kg m^{-3} . The ridge axis is indicated by the *double lines*. Segment boundaries identified from magnetic data [16] are marked by *black* or *white thick lines*. See text for details on the rotation of grids, and on calculations of the RMBA and crustal thickness maps.

tion of the relationship between gravity and bathymetry in the spectral domain [17,18]. Spectral transfer functions (admittance and coherence) between gravity and bathymetry can also be used to estimate the effective elastic thickness (EET) of the oceanic lithosphere [19–21]. In this paper we test a simple conceptual model for on-axis crustal construction and off-axis modification using isochron and flow-line data of residual gravity and bathymetry of the northern MAR. The primary high-resolution data were collected on the western flank of the MAR in 0–25 Ma old crust (25.5–27.5°N) [16] and along the MAR axis at 24–30°N. Statistical and coherence analyses of these data suggest that the oceanic crust is modified by tectonic extension at the spreading center.

2. Conceptual model

The systematic gravity patterns observed at slow spreading ridge segments are summarized in Fig. 1a. Off-axis zones of relatively thin crust (positive residual gravity) are mainly found on crust formed at inside corners of ridge-offset intersections, while zones of relatively thick crust (negative gravity) are found along segment centers. This pattern of gravity highs and lows is relatively continuous off-axis and shows a wavy pattern with varying amplitude, which has been previously attributed to temporal variations in magmatic crustal emplacement [11,13,14] (Fig. 1a). The shallowest seafloor in crust > 1–2 Ma is often not located at the center of the segment as along the axis (Fig. 1b), but instead at the ICs, and the gravity highs are often displaced from the trace of the discontinuity and centered at ICs (isochron profile in Fig. 1c). The model proposed in Fig. 1 indicates that off-axis RMBA highs mark the locus of tectonic thinning at inside corners [12] rather than the paleoposition of ridge offsets as proposed by Rommeveaux et al. [14]. This interpretation is consistent with substantial tectonic uplift through low-angle faults at ICs [22,23], the increase in spacing and throw of faults from segment midpoints towards segment ends [24,25], and the clustering of microearthquakes at ICs [26]. In this study we will test this simple model using on- and off-axis residual gravity and bathymetry data.

3. Data reduction

The data used encompass the MAR axis between the Kane and Atlantis fracture zones (FZs) and extend to 25 Ma crust off axis on the west flank of the MAR between 25.5° and 27.5°N (Fig. 2). The data comprise along-axis surveys [4,28] and the off-axis survey in the ONR Acoustic Reverberations Special Research Program (ARSRP) area [16]. Also included are data from the TAG area [29], and from the MAR axis north and south of the Kane FZ [30,31]. Details on track coverage, navigation, and data processing are given in the above references.

Data from the ARSRP area have been rotated, for purposes of presentation and data analysis, into an across- and along-axis coordinate system (Fig. 3). The spreading direction at 26°N predicted by the plate model NUVEL-1 [32] is N100°. The magnetic lineations and abyssal hill orientations mark a counter-clockwise change of $\sim 9^\circ$ in plate motion at 22–24 Ma [16] that is recorded by the trace of the Kane FZ [33]. We remapped the data by clockwise rotation of the crust younger than 20 Ma by 10° and the crust older than 20 Ma by 19° , and resampled it in the new rotated coordinate system (Fig. 3). In this rotated coordinate system, the ridge axis, abyssal hills and magnetic lineations are sub-parallel to the

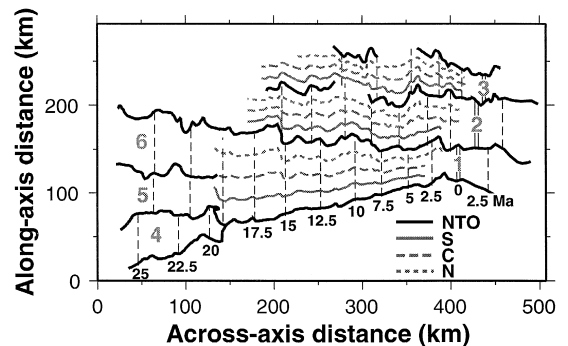


Fig. 4. Location of isochron and flow-line profiles along the north (N), central (C) and south (S) sections of ridge segments. Traces of non-transform offsets (NTOs) are also identified. These profiles were used to calculate the coherence between residual gravity and bathymetry and to perform statistical analyses. Non-transform segment offsets (NTOs) are marked by *bold lines*, and are identified from magnetic anomalies [17]. The *small numbers* indicate crustal isochron ages in Ma, and the *gray numbers* mark different active and extinct segments.

y-axis, and the direction of spreading is parallel to the x-axis (Fig. 3a). In the rotated maps at $x \approx 150$ km a small strip of data overlap and gap exists south and north of the point of rotation, respectively (Fig. 3a). This strip was not included in any of the profiles used in the analysis (Fig. 4). The magnetic data on the MAR at 28–29°N, immediately north of the study area, show plate motion changes of less than $\pm 10^\circ$ during the last 10 Ma [34]. As these changes in spreading direction were relatively small, short-lived and local, they were not incorporated in the remapping scheme.

The reduction of free-air gravity anomaly (FAA) to obtain mantle-Bouguer (MBA) and residual mantle-Bouguer anomalies (RMBA) followed the procedures of Kuo and Forsyth [3]. The gravity effects from the water–crust and crust–mantle interfaces were calculated using the upward continuation method of Parker [35], and correction for the thermal cooling of the mantle was calculated using a 3-D passive mantle upwelling model [36] (model parameters are given in Table 1). The MBA and RMBA corrections were subtracted from the FAA at each point along ship tracklines. The anomalies were then gridded to obtain the RMBA map in Fig. 3b. The RMBA arises from differences between the modeled and actual densities of the crust and mantle, and from variations in crustal thickness. Mantle density variations associated with thermal anomalies are relatively small and therefore most of the RMBA reflects thickness or density variations of the crust [37,38].

Relative crustal thickness is calculated by downward continuation of the RMBA [39]. Convergence

Table 1
Model parameters used in gravity calculations

Parameter	Value
Gravitational constant ($\text{N m}^2 \text{kg}^{-2}$)	6.6673×10^{-11}
Gravitational acceleration ($\text{m}^2 \text{s}^{-1}$)	9.80
Water density (kg m^{-3})	1030
Crustal density (kg m^{-3})	2700
Mantle density (kg m^{-3})	3300
Crustal thickness (km)	6
Half spreading rate (km Ma^{-1})	13
Thermal boundary layer thickness (km)	100
Asthenospheric temperature ($^\circ\text{C}$)	1350
Coefficient of thermal expansion ($^\circ\text{C}^{-1}$)	3.2×10^{-5}

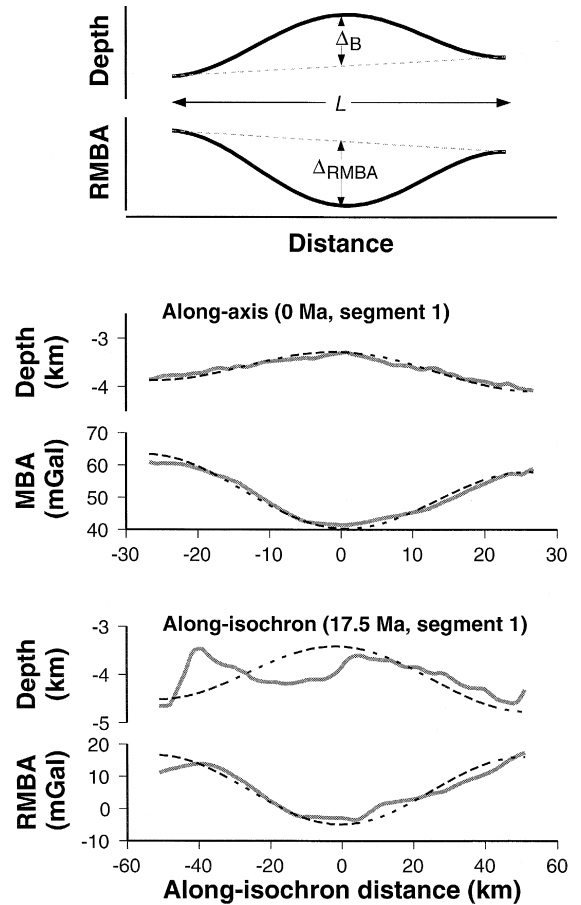


Fig. 5. (a) Theoretical cosine curves used to model the along-axis bathymetry and gravity within a segment. Once linear trends (dashed) are removed, the depth and RMBA curves can be parametrized by cosine functions with the form $y = \pm \Delta / \cos(2\pi x / L) + a + mx$, where a and m correspond to the origin and slope of the linear trend, respectively, and Δ characterizes the amplitude of segment-scale variations.

(b) Example of data and cosine function approximation to the zero-age profile from segment 1.

(c) Example of data and cosine function approximation to an isochron profile (17.5 Ma, segment 1).

of the solution during inversion is ensured using a low-pass filter with cosine tapering beginning at 35 km wavelength and ending at 25 km. Since crustal thickness calculations are non-unique, two alternative models of density structure are presented. Model A has a single crustal layer with a density $\rho_c = 2700$ kg m^{-3} . Model B has two layers, with an upper crust of 2 km constant thickness and density $\rho_c = 2600$ kg

m^{-3} , and a lower crust of variable thickness and $\rho_c = 2800 \text{ kg m}^{-3}$. The relative crustal thickness maps are shown in Fig. 3c and d (models A and B, respectively). Model B is intended to reflect more accurately the recent seismic observations suggesting systematic thinning of the lower crust (layer 3) with the upper crust (layer 2) maintaining a relatively constant thickness [40,41]. Previous gravity analyses using a crust of constant density (model A) underestimate crustal thickness variations with respect to seismic methods [40,41]. However, model B produces larger relative crustal thickness variations than model A (± 3.5 and ± 2.0 km) since the density contrast at the crust–mantle interface is smaller in model B ($\Delta\rho = 500$ and 600 kg m^{-3}).

4. Variations in segment-scale bathymetry and gravity structure

The effect of tectonic extension at the spreading center can be investigated by comparing off-axis residual gravity and bathymetry data with those along the zero-age crust. The isochron profiles chosen for analysis are spaced at 2.5 Ma intervals, from 0 to 25 Ma old crust, as determined from magnetic anomalies [16] (Fig. 4). Because our main objective is to quantify the segment-scale variability, we remove a linear trend in the bathymetry and RMBA profiles that might be associated with processes at wavelengths longer than the segment length (i.e., regional effect of the Azores hot spot [6]). The detrended curves are then parametrized by segment length L , amplitude of along-axis bathymetric variation Δ_B within a segment, and amplitude of the RMBA Δ_{RMBA} using a cosine curve (Fig. 5). The correlation coefficients of the linear fit between the model and the data in a least-squares sense are calculated for the bathymetry and gravity (r_B and r_{RMBA} , respectively), and for the fit between gravity and bathymetry ($r_{B-\text{RMBA}}$). The calculated parameters L , Δ_B and Δ_{RMBA} , the correlation coefficients r_B , r_{RMBA} , and $r_{B-\text{RMBA}}$, and the confidence level of the fits using a Student's t -test [42] are given in Table 2.

The results in Table 2 and Fig. 6 indicate that the zero-age crustal structure formed at the ridge axis is modified by tectonic extension at the spreading cen-

ter. A positive and well-resolved correlation (confidence level ≥ 0.90) indicates that the model explains satisfactorily the data; well-resolved negative correlations indicate that the data are anticorrelated with the model and therefore cannot be explained by them. Out of 22 zero-age profiles, 15 and 16 of the bathymetry and gravity profiles are explained by the cosine model, and 14 show positive and well-resolved correlation between bathymetry and gravity. In contrast, 19 out of the 31 off-axis bathymetry and gravity profiles are explained by the cosine model, and only 13 show positive and well-resolved correlation between bathymetry and gravity (Table 2). There is also a marked difference in the segment length L vs. Δ_B and Δ_{RMBA} relationships between the zero-age and off-axis profiles (Fig. 6) for those profiles that are properly explained by the cosine model; the zero-age data show a well-resolved positive correlation of Δ_B and Δ_{RMBA} with L , consistent with earlier studies [4,6] that is not found on the off-axis profiles. For a given segment length, off-axis Δ_B values appear to be systematically higher than the on-axis ones (Fig. 6a) while off-axis Δ_{RMBA} values tend to be lower (Fig. 6b).

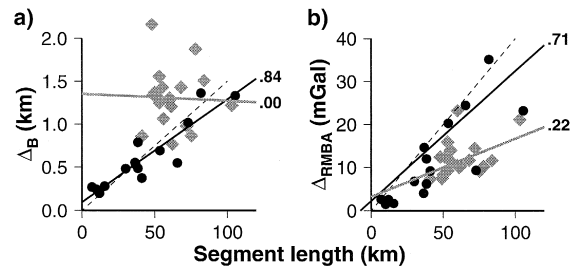


Fig. 6. (a) Measured segment-scale variations in bathymetry (Δ_B) vs. segment length L .

(b) Measured segment-scale variations in gravity (Δ_{RMBA}) vs. segment length L .

The zero-age data (solid circles) display a linear increase in amplitude with segment length. In contrast, the off-axis isochron data (gray diamonds) do not display any clear trends. The lines are the best fit to the data, and the numbers correspond to the correlation coefficient r^2 . The dashed lines correspond to the trends reported for the MAR segments at 28° – 30°N [4] and 33° – 40°N [6]. Only data that fit the model with a confidence level > 0.9 are plotted.

Table 2
Results of statistical analysis

Segment	L (km)	Δ_B (m)	r_B	Conf. level	Δ_{RMBA} (mGal)	r_{RMBA}	Conf. level	$r_{B-\text{RMBA}}$	Conf. level
<i>Present-day axis:</i>									
SK-A	106	1335	0.77	> 0.99	23.22	0.17	< 0.01	0.37	> 0.99
KA-A	90	891	-0.18	< 0.01	28.26	0.57	> 0.99	0.36	0.97
KA-B	15	283	0.96	> 0.99	1.67	-0.59	0.77	-0.63	0.86
KA-C	12	200	0.86	> 0.99	2.62	0.94	> 0.99	0.82	> 0.99
KA-4	10	245	0.97	> 0.99	1.45	-0.95	> 0.99	-0.97	> 0.99
KA-D	54	692	0.99	> 0.99	20.28	0.99	> 0.99	0.98	> 0.99
KA-E	37	551	0.59	> 0.99	4.04	0.60	> 0.99	0.08	< 0.01
KA-F	39	485	0.65	> 0.99	11.99	0.79	> 0.99	0.72	> 0.99
KA-G	34	795	-0.74	> 0.99	3.69	0.56	0.99	0.01	< 0.01
KA-H	11	272	-0.71	0.86	3.89	0.85	0.98	-0.81	0.97
KA-I	39	788	0.85	> 0.99	6.21	0.90	> 0.99	0.93	> 0.99
KA-J	37	530	0.91	> 0.99	14.69	0.79	> 0.99	0.89	> 0.99
KA-K	30	480	0.83	> 0.99	6.81	0.92	> 0.99	0.77	> 0.99
KA-L	7	269	0.88	0.98	2.69	0.76	0.97	0.72	0.96
KA-M	37	394	-0.46	0.56	8.40	-0.68	> 0.99	-0.10	< 0.01
KA-N	45	687	-0.87	> 0.99	11.87	-0.08	< 0.01	0.47	0.76
KA-O	41	375	0.96	> 0.99	9.15	0.79	> 0.99	0.69	> 0.99
KA-P	12	105	-0.18	< 0.01	1.86	-0.73	0.65	0.38	< 0.01
KA-Q	19	242	-0.95	> 0.99	4.36	0.91	> 0.99	-0.86	> 0.99
KA-R	65	548	0.95	> 0.99	24.51	0.94	> 0.99	0.92	> 0.99
KA-S	82	1363	0.91	> 0.99	35.17	0.97	> 0.99	0.91	> 0.99
NA-A	73	1018	0.81	> 0.99	9.30	0.74	> 0.99	0.40	0.99
<i>Off-axis isochron:</i>									
OA-1-2.5	53	1557	0.88	> 0.99	15.98	0.90	> 0.99	0.77	> 0.99
OA-1-5.0	48	2164	0.57	> 0.99	12.45	0.85	> 0.99	0.43	0.93
OA-1-7.5	55	1431	0.84	> 0.99	14.02	0.57	> 0.99	0.05	< 0.01
OA-1-10.0	78	1877	0.77	> 0.99	10.23	0.80	> 0.99	0.35	0.92
OA-1-12.5	84	1510	0.56	> 0.99	11.66	0.84	> 0.99	0.51	> 0.99
OA-1-15.0	85	1219	-0.30	0.63	4.32	0.87	> 0.99	-0.47	0.87
OA-1-17.5	103	1224	0.47	> 0.99	21.21	0.97	> 0.99	0.34	0.97
OA-1-20.0	113	1148	0.23	0.05	24.50	0.92	> 0.99	0.06	0.01
OA-1-2.5	60	1277	0.88	> 0.99	23.24	0.82	> 0.99	0.60	> 0.99
OA-2-2.5	72	979	0.86	> 0.99	14.52	-0.55	> 0.99	-0.46	> 0.99
OA-2-5.0	60	1304	0.73	> 0.99	10.44	0.77	> 0.99	0.69	> 0.99
OA-2-7.5	49	997	0.26	0.23	4.87	-0.43	0.92	-0.87	> 0.99
OA-2-10.0	51	1326	0.98	> 0.99	12.47	0.6	0.99	0.50	0.98
OA-2-12.5	65	938	-0.27	0.14	15.82	0.04	0.56	-0.60	> 0.99
OA-2-15.0	68	1430	0.69	> 0.99	11.75	0.28	0.15	-0.21	0.19
OA-2-17.5	61	1209	0.90	> 0.99	10.02	0.59	> 0.99	0.29	0.13
OA-2-20.0	57	853	0.20	< 0.01	8.38	-0.63	> 0.99	-0.51	> 0.99
OA-2-22.5	48	317	-0.02	< 0.01	7.46	-0.68	> 0.99	-0.41	0.89
OA-2-2.5	66	1472	-0.67	> 0.99	10.73	0.26	0.18	-0.18	0.24
OA-3-2.5	37	289	-0.26	0.18	6.35	0.68	> 0.99	0.16	0.08
OA-3-5.0	56	1064	0.9	> 0.99	11.22	0.82	> 0.99	0.70	> 0.99
OA-3-7.5	53	1251	0.69	> 0.99	9.29	0.63	> 0.99	0.50	0.98
OA-3-10.0	54	713	-0.49	0.89	11.56	-0.06	< 0.01	-0.04	< 0.01
OA-3-12.5	39	541	-0.79	> 0.99	9.58	-0.89	> 0.99	0.50	0.95
OA-4-20.0	41	862	0.77	> 0.99	7.31	-0.91	> 0.99	-0.73	> 0.99
OA-4-22.5	49	1347	0.53	0.98	7.51	0.80	> 0.99	0.08	0.60

Table 2 (continued)

Segment	L (km)	Δ_B (m)	r_B	Conf. level	Δ_{RMBA} (mGal)	r_{RMBA}	Conf. level	r_{B-RMBA}	Conf. level
<i>Off-axis isochron:</i>									
OA-4-25.0	62	768	0.58	> 0.99	10.39	0.60	> 0.99	0.75	> 0.99
OA-5-22.5	50	490	-0.64	> 0.99	11.33	-0.01	< 0.01	-0.41	0.90
OA-5-25.0	50	1370	0.71	> 0.99	8.24	-0.59	> 0.99	-0.94	> 0.99
OA-6-22.5	60	186	-0.72	> 0.99	4.95	0.95	> 0.99	-0.62	> 0.99
OA-6-25.0	75	865	0.79	> 0.99	9.15	0.87	> 0.99	0.86	> 0.99

Segments: NA = north of Atlantis; KA = Kane-Atlantis; SK = south of Kane; OA = off axis. Letters on along-axis profile names in order from S to N. Numbers on off-axis profiles are segment number-age in Ma as given in Fig. 4. KA-F, KA-I, and KA-J correspond to segments 1, 2, and 3 in Fig. 4, respectively. L = segment length; Δ_B = amplitude of bathymetry; r_B = correlation coefficient of model and bathymetry; Δ_{RMBA} = amplitude of residual gravity; r_{RMBA} = correlation coefficient of model and residual gravity; r_{B-RMBA} = correlation coefficient of bathymetry and residual gravity. Conf. level: Student's t -test confidence level of r [42]; confident levels in italic.

5. Contrasts in coherence

The correlation between residual gravity and bathymetry can be estimated in the spectral domain by the squared coherence (γ^2):

$$\gamma^2 = \langle G \cdot H^* \rangle^2 / \langle G \cdot G^* \rangle \langle H \cdot H^* \rangle$$

where G and H are the Fourier coefficients for the residual gravity and bathymetry, respectively; the triangular brackets indicate averaging over individual spectral bands; and the asterisk denotes the complex conjugate. In the presence of an elastic plate, residual gravity and bathymetry are expected to be correlated at long wavelengths and therefore have a coherence approaching 1. At short wavelengths, however, the topography can be dynamically maintained and therefore low coherence values approaching 0 are expected. In an idealized model, the wavelength of the transition from low to high coherence depends primarily on the effective elastic thickness (EET) of the lithosphere, and is relatively insensitive to the ratio of top to bottom loading (f) of the plate [43]. Other spectral parameters, such as admittance [19], are strongly dependent on f in addition to the EET, and may yield anomalously low flexural rigidities depending on the assumed value of f [43]. Coherence is thus preferred over admittance in our analysis. The coherence functions, the error of the coherence estimate, and confidence level were calculated using a section-averaged, multiple-window technique with jackknifed error estimates as described by Chave et al. [44] and Thomson and Chave [45]. As opposed to band-averaging methods, the multiple window

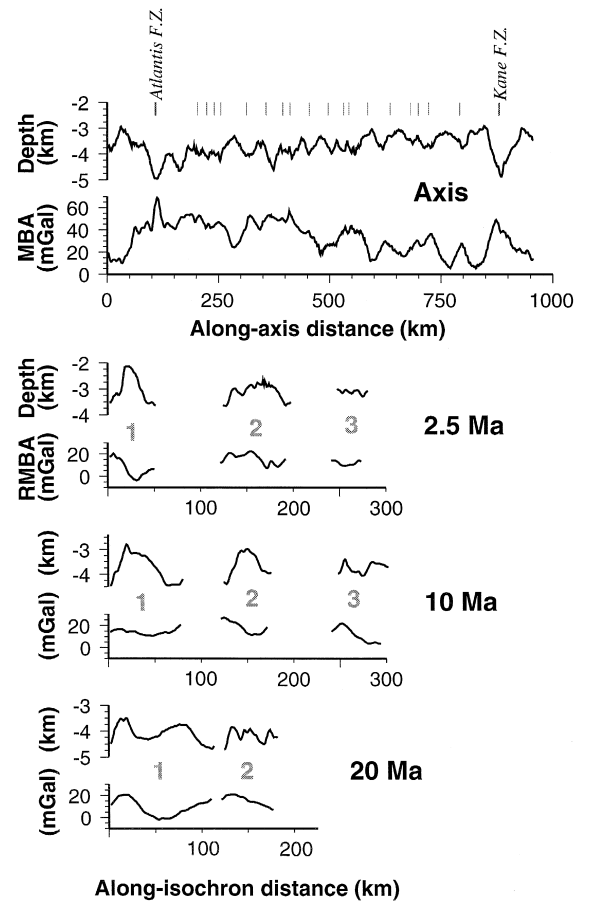


Fig. 7. Bathymetry and MBA profiles along the ridge axis, and residual bathymetry and RMBA along isochron profiles. In the zero-age profile, non-transform offsets are marked by thin vertical lines and transform faults by the labeled lines. Numbers on the isochron profiles mark the segment number (Fig. 4).

coherence method is not dominated by spectral leakage, and thus yields statistically robust coherence estimates [44].

We performed spectral analyses on residual gravity and bathymetry profiles along the zero-age crust, off-axis isochrons, and flow-lines of each of the segments in study area (Fig. 4). Due to the complex segmentation patterns and the relatively small size of our study area ($\sim 500 \times 200$ km), 2-D coherence analysis is impractical as it would provide flexural rigidity estimates over a wide range of crustal ages and different ridge segments. Long profiles of axial and off-axis data were constructed by joining data of a given age from the different segments and interpolating over 5 km [18] (Fig. 7); the axial profile extends over ~ 900 km from south of the Kane FZ ($\sim 22^\circ 40' N$) to north of the Atlantis FZ ($30^\circ 30' N$). The north, south, and central flow-lines are located at 25%, 50%, and 75%, respectively, of the distance between the two non-transform offsets bounding each segment (Fig. 4). The south and north flow-lines on segment 1 (Fig. 4) sample IC and OC crust, respectively. The north flow-line on segment 2 and the

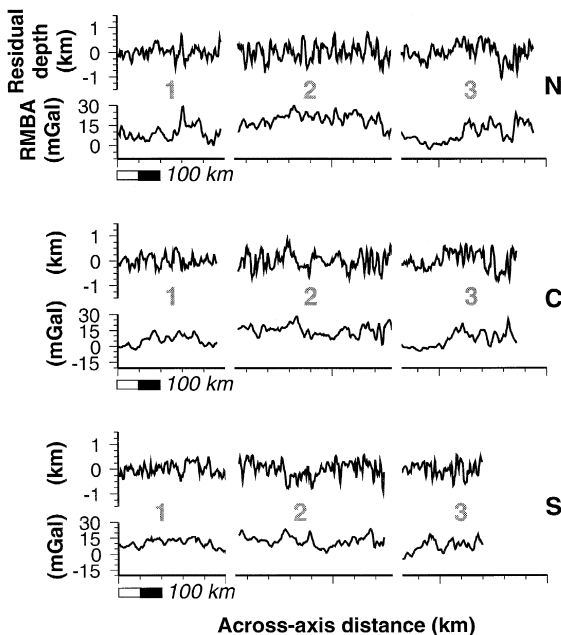


Fig. 8. Flow-line profiles of residual bathymetry and RMBA through the north (N), center (C), and south (S) sections of segments (see Fig. 4 for location of profiles).

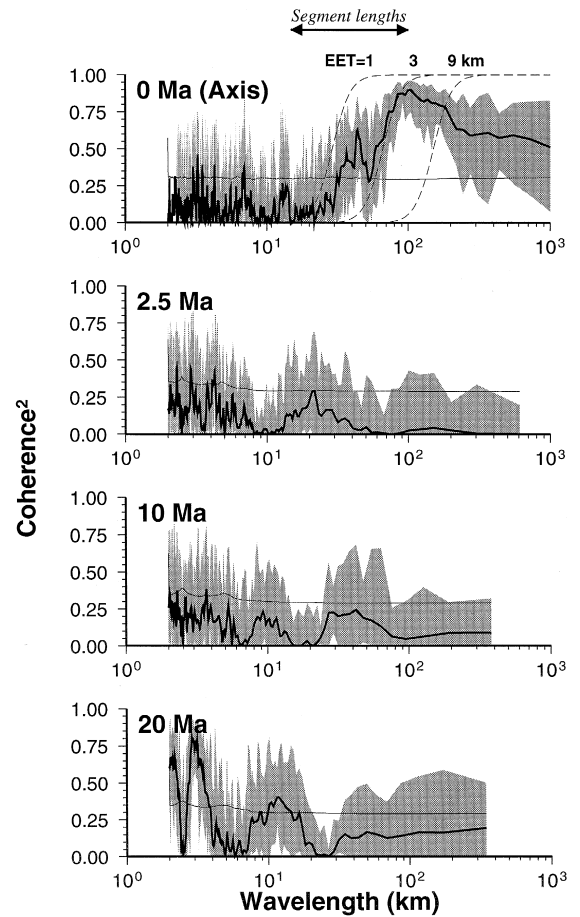


Fig. 9. Computed coherence functions between residual gravity and bathymetry along the zero-age crust and selected crustal isochrons of 2.5, 10, and 20 Ma from Fig. 4. Note that off-axis data show no coherence at any wavelengths, indicating that the crustal structure created at the ridge axis is significantly disrupted by tectonic processes within a very short distance from the ridge axis. Theoretical coherence functions [43] for an elastic plate with effective thickness of 1, 3, and 9 km are also shown on the zero-age profile. Shading corresponds to 1σ of data uncertainties and the thin horizontal line marks the zero confidence level in the coherence analysis. The double arrow on the axial coherence indicates the range in length of segments on the zero-age profile.

south flow-line on segment 3 sample both IC and OC crust, as the polarity of the discontinuity changes at ~ 12 Ma [16] (Fig. 4). Crust within the axial valley (age < 2.5 Ma) was not included in flow-line profiles; the rift valley may be dynamically maintained and its inclusion could result in reduced co-

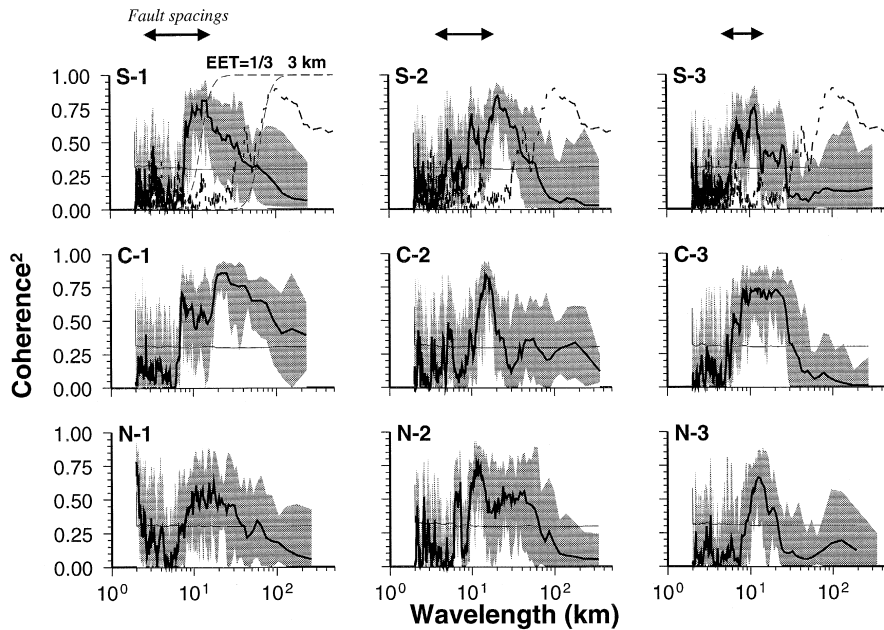


Fig. 10. Coherence functions for flow-line profiles along the north (*N*), center (*C*), and south (*S*) sections of segments 1, 2, and 3 of Fig. 4. The coherence for zero-age crust (*dashed*) is shown in the top panels for comparison. Theoretical coherence curves for elastic plate thicknesses of 1/3 and 1 km are also shown in the top left panel for comparison. The *horizontal double arrows* mark the range of fault spacing [48] in each of the segments. Other conventions are the same as in Fig. 9.

herence [18]. For each flow-line bathymetric profile, a square-root-of-age curve was subtracted to obtain residual bathymetry (Fig. 8). Coherence on the flow-line profiles was calculated using the residual bathymetry and the RMBA to remove variations due to thermal cooling while maintaining other long-wavelength signals (i.e., off-axis loading). Coherence between bathymetry and MBA is essentially identical to the coherence between residual bathymetry and the RMBA at the sampled wavelengths, and differences may only be found at long wavelengths (> 200 km).

5.1. Zero-age coherence

The coherence function between bathymetry and MBA along the ridge axis yields an EET of 1–3 km for the zero-age crust (Fig. 9). The transition from coherence of ~ 0 to ~ 0.8 occurs between wavelengths of 20–100 km, and is bracketed by the theoretical coherence functions for a 2-D elastic plate [43] with EET of 1–3 km. Coherence decreases somewhat at wavelengths > 100 km. We have as-

sumed a top-to-bottom loading ratio f of 1. Our result is similar to the EET of ~ 2 km obtained by Neumann and Forsyth [18] along a zero-age profile that combines several segments from the north and south MAR.

The length of the zero-age profile is ~ 900 km, which is considerably longer than that of off-axis isochron profiles (< 400 km). To test the effect of profile length on the coherence, we calculated the coherence on four sub-profiles (each ~ 240 km long) of the zero-age profile. For each sub-profile, we obtained EET values of 1–4 km, similar to the 1–3 km values obtained for the 900 km long profile. The maximum coherence in all sub-profiles was ~ 0.6 , always above the confidence level, but lower than the ~ 0.8 shown in Fig. 9 for the 900 km long profile.

5.2. Off-axis isochron coherence

The coherence functions for all off-axis isochron profiles show that residual gravity and bathymetry in crust older than ~ 2 Ma are systematically uncorre-

lated at all wavelengths. This lack of coherence can be seen by comparing the coherence for the ridge axis data with those for isochrons at 2.5, 10, and 20 Ma (Fig. 9). The calculated coherence is lower than the confidence level except for wavelengths < 4 km in all profiles and at ~ 10 km in the 20 Ma profile. The coherence peaks at wavelengths < 4 km can be attributed to noise because wavelengths shorter than the water depth (~ 4 km) were filtered by upward continuation of the gravity. The coherence peak at wavelengths of ~ 10 km in the 20 Ma profile has large errors associated, suggesting that these values may not be significant.

5.3. Flow-line coherence

The observed coherence functions for profiles along flow-lines over the crust in the north, center and south of the three segments (N, S, and C, respectively; Fig. 10) also differs substantially from that of the axial profile. The transition from uncorrelated to correlated bathymetry occurs at wavelengths of 7–15 km on average. At wavelengths > 20 –100 km, bathymetry and gravity become uncorrelated in all flow-line profiles.

6. Discussion

6.1. Interpretation of isochron coherence results

The ridge axis coherence may reflect the variability in spreading segment length (arrow in Fig. 9, top) rather than the true elastic plate thickness of the axial valley floor. The measured coherence along the ridge axis is controlled mostly by the systematic correlation between gravity and bathymetry at segment scale (Fig. 7a) that may arise from focused magmatic accretion at segment centers. The transition from no coherence to high coherence on the zero-age profile occurs at ~ 10 –100 km, which is similar to the observed segment lengths (Table 2), and may coincide fortuitously with that of a flexural model with EET values of ~ 1 –3 km (Fig. 9).

The coherence functions along isochrons in crust age of 2.5 Ma and older differ substantially from that of the zero-age crust (Fig. 9), in that they show no coherence at wavelengths < 300 km, which is the

maximum length of off-axis isochron profiles. The lack of coherence is consistent with the lack of correlation between segment length and segment-scale anomalies in off-axis data (Fig. 6), and is best attributable to the modification of the crustal structure by tectonic extension. Other effects, such as differential thermal subsidence across ridge offsets [46], are expected to be small because the offsets are short. Coherence may exist at wavelengths > 300 km, but cannot be resolved without out data. Since isochron profiles in crust ages of 2.5–25 Ma display similar patterns in residual gravity, bathymetry, and coherence (Figs. 6 and 9; Table 2), it is expected that the transition from the unfaulted crust to the significantly faulted crust must occur within short distance of the ridge axis (1–2 Ma crust).

The degree of crustal modification appears to vary both temporally and spatially. We note that several of the off-axis isochron profiles show a pattern similar to the zero-age profiles (Table 2), indicating that the axial crustal structure may sometimes be maintained off axis. Based on the spacing of isolated residual gravity peaks along off-axis traces of inside corner crust, it was previously proposed that the formation of inside corner terrain may be discontinuous in time [12]. Although some of the off-axis isochron profiles show a crustal structure similar to the axial profiles, the length–amplitude correlation observed on-axis is not maintained off-axis (Fig. 6), indicating that even in those cases modification of the axial crust has occurred. Tectonic extension must also vary along rift valley walls and among segments to result in decorrelation between residual gravity and bathymetry in off-axis isochrons (Fig. 9).

6.2. Flow-line coherence and faulting

The lack of coherence at long wavelengths on the flow-line profiles (Fig. 10) is not consistent with flexural models of an elastic plate that predict high coherence at long wavelengths [43]. In addition, the calculated EET for all of the flow-line profiles is < 0.3 –0.5 km, substantially smaller than the 1–3 km determined for the ridge axis (dashed lines in Fig. 10) even though the EET of the oceanic lithosphere is expected to increase with age [47]. Therefore, other models must be invoked to explain the observed transition from non-significant to significant

coherence at anomalously short wavelengths of 7–15 km.

Faulting along rift valley walls can reshape the crust substantially before it is rafted off axis. Fault spacing varies along the length of MAR segments, ranging from ~ 1 –3 km at outside corners and segment midpoints to ~ 3 –10 km at inside corners [25]. The typical fault spacing estimated from side-scan sonar at the midpoints of the three segments is 0.8–1.5 km, and the maximum abyssal hill width of the same segments is ~ 18 km [48]. Abyssal hills along the MAR are interpreted to have a tectonic origin [25,48], and their width may be an indirect measure of the spacing of larger faults. The range in fault spacing along each segment is indicated in Fig. 10 by the horizontal double arrows, which in all cases overlap with the transition from no to significant coherence. Thus, the bathymetry is strongly correlated with residual gravity at wavelengths similar to the abyssal hill spacing, i.e. major fault spacing. Synthetic modeling suggests that faulting can cause anomalies in both seafloor topography and residual gravity [12], and thus coherence at wavelengths similar to the fault spacing (1– ~ 20 km) is expected. The shorter wavelengths (≤ 4 km) of the residual gravity signal are filtered by upward continuation from the crust to the sea surface. Thus, the observed transition from no coherence to high coherence at ~ 7 –15 km on flow-line profiles may be caused by faulting rather than reflecting a thin elastic plate with EET values of < 0.3 –0.5 km.

The lack of coherence at wavelengths ≥ 100 km in the flow-line profiles is not predicted by flexural models. Temporal variability in magmatic accretion may result in across-axis variations in crustal thickness at time scales of 2–9 Ma [11,13,14], corresponding to intermediate wavelengths of 25–100 km. However, there is no identified magmatic or tectonic process that will produce morphology and crustal thickness variations at wavelengths > 100 km (i.e., > 10 Ma), and consequently, low coherence due to lack of power may be expected at long wavelengths.

7. Conclusions

Spectral and statistical analyses of residual gravity and bathymetry data of the Mid-Atlantic Ridge indi-

cate that the crustal structure at the ridge axis is strongly modified by tectonic extension at the spreading center. Seafloor along the axis is systematically elevated and the crust thicker at the segment midpoint than at the segment ends, suggesting focused magmatic accretion at segment centers [3,4]. In contrast, seafloor older than 2–3 Ma is usually the shallowest at inside corners of ridge-offset intersections, where positive residual gravity anomalies indicate tectonically thinned crust. Evidence for this tectonic modification can also be found from spectral and statistical analyses of residual gravity and bathymetry. The zero-age crust profile displays high coherence at wavelengths greater than 20 km, which corresponds to the characteristic length of ridge segments and coincides with an effective elastic plate thickness of 1–3 km. In contrast, isochron profiles outside the rift valley show no significant coherence at all wavelengths. Furthermore, while there is a marked positive linear correlation between segment length and the segment-scale anomalies in the zero-age crust, such correlation is absent in the off-axis isochron profiles. These results are consistent with substantial tectonic modification of the crust off-axis. The transition from the axial to the off-axis crustal structure occurs at 1–2 Ma crust, along the rift-valley walls.

The effect of tectonic extension is also observed on flow-line profiles and is inferred from fault models. Synthetic models suggest that faults may result in residual gravity and bathymetric anomalies correlated at wavelengths equal the fault spacing. The transition from no coherence to high coherence on the flow-line profiles is observed at wavelengths of ~ 7 –15 km, which overlaps with the typical fault spacing values of ~ 1 –20 km [25,48] in the study area. The calculated coherence is not consistent with an elastic plate model, as the calculated effective elastic plate thickness is < 0.3 –0.5 km, lower than the ~ 1 –3 km inferred for the zero-age crust. Consequently, interpretation of the effective elastic plate thickness from coherence must be done with caution, as several processes, such as faulting and focused magmatic accretion, may result in a high degree of correlation between residual gravity and bathymetry. The off-axis crustal structure records not only the on-axis magmatic processes [49] but also the near-axis tectonic processes that further modify the crust.

Acknowledgements

This study benefited from discussion with and suggestions from R. Detrick, G. Hirth, K. Hodges, G. Ito, G. Jaroslow, D. Lizarralde, D. Smith, M. Tivey, and B. Tucholke. A. Chave is specially acknowledged for providing codes for robust spectral estimations as well as comments and suggestions. The paper also benefited from reviews from J. Goff, T. Henstock, and C. Small. The GMT software [50] was extensively used in this study. This work was supported by NSF grant OCE-9300708, and the AR-SRP data were acquired with funding from ONR N00014-90-J-1621. Contribution 9270 of the Woods Hole Oceanographic Institution.

References

- [1] H. Schouten, K.D. Klitgord, J.A. Whitehead, Segmentation of mid-ocean ridges, *Nature* (London) 317 (1985) 225–229.
- [2] J.C. Sempéré, J. Lin, H.S. Brown, H. Schouten, G.M. Purdy, Segmentation and morphotectonic variations along a slow-spreading center: the Mid-Atlantic Ridge (24°N–30°40'N), *Mar. Geophys. Res.* 15 (1993) 153–200.
- [3] B.Y. Kuo, D.W. Forsyth, Gravity anomalies of the ridge-transform system in the South Atlantic between 31° and 34°S: Upwelling centers and variations in crustal thickness, *Mar. Geophys. Res.* 10 (1988) 205–232.
- [4] J. Lin, G.M. Purdy, H. Schouten, J.-C. Sempéré, C. Zervas, Evidence from gravity data for focused magmatic accretion along the Mid-Atlantic Ridge, *Nature* (London) 344 (1990) 627–632.
- [5] M. Tolstoy, A.J. Harding, J.A. Orcutt, Crustal thickness on the Mid-Atlantic ridge: Bull's eye gravity anomalies and focused accretion, *Science* 262 (1993) 726–729.
- [6] R.S. Detrick, H.D. Needham, V. Renard, Gravity anomalies and crustal thickness variations along the Mid-Atlantic Ridge between 33°N and 40°N, *J. Geophys. Res.* 100 (1995) 3767–3787.
- [7] T.J. Henstock, R.S. White, J.H. McBride, Along-axis variability in crustal accretion at the Mid-Atlantic Ridge: Results from the OCEAN study, *J. Geophys. Res.* 101 (1996) 13673–13688.
- [8] J.A. Whitehead, H.J.B. Dick, H. Schouten, A mechanism for magmatic accretion under spreading centres, *Nature* (London) 312 (1984) 146–148.
- [9] K. Crane, The spacing of rift axis highs: dependence upon diapiric processes in the underlying asthenosphere?, *Earth Planet. Sci. Lett.* 72 (1985) 405–414.
- [10] J.P. Severinghaus, K.C. Macdonald, High inside corners at ridge-transform intersections, *Mar. Geophys. Res.* 9 (1988) 353–367.
- [11] B.E. Tucholke, J. Lin, A geological model for the structure of ridge segments in slow-spreading ocean crust, *J. Geophys. Res.* 99 (1994) 11937–11958.
- [12] J. Escartín, J. Lin, Ridge offsets, normal faulting, and gravity anomalies of slow-spreading ridges, *J. Geophys. Res.* 100 (1995) 6163–6177.
- [13] J. Lin, B.E. Tucholke, M.C. Kleinrock, Evidence from gravity and morphology for long-term variability in magmatic vs. tectonic extension at the Mid-Atlantic Ridge, *Eos* (Trans. Am. Geophys. Union) 74 (1993) 303, abstract.
- [14] C. Rommeveaux, C. Deplus, P. Patriat, J.-C. Sempéré, Three-dimensional gravity study of the Mid-Atlantic Ridge: Evolution of the segmentation between 28° and 29°N during the last 10 m.y., *J. Geophys. Res.* 99 (1994) 3015–3029.
- [15] J.E. Pariso, J.-C. Sempéré, C. Rommeveaux, Temporal and spatial variations in crustal accretion along the Mid-Atlantic Ridge (29°–31°30'N) over the last 10 my.: Implications from a three-dimensional gravity structure, *J. Geophys. Res.* 100 (1995) 17781–17794.
- [16] B.E. Tucholke, J. Lin, M.C. Kleinrock, M.A. Tivey, T. Reed, J. Goff, G. Jaroslow, Segmentation and crustal structure of the western Mid-Atlantic ridge flank, 25°30'–27°10'N and 0–29 M.y., *J. Geophys. Res.* 102 (1997) 10203–10223.
- [17] E.M. Parmentier, D.W. Forsyth, Three-dimensional flow beneath a slow-spreading ridge axis: A dynamic contribution to the deepening of the median valley toward fracture zones, *J. Geophys. Res.* 90 (1985) 678–684.
- [18] G.A. Neumann, D.W. Forsyth, The paradox of the axial profile: Isostatic compensation along the axis of the Mid-Atlantic Ridge?, *J. Geophys. Res.* 98 (1993) 17891–17910.
- [19] D. McKenzie, C. Bowin, The relationship between bathymetry and gravity in the Atlantic Ocean, *J. Geophys. Res.* 81 (1976) 1903–1915.
- [20] J.R. Cochran, An analysis of isostasy in the world's oceans 2 Midocean ridge crests, *J. Geophys. Res.* 84 (1976) 4713–4730.
- [21] D.K. Blackman, D.W. Forsyth, Isostatic compensation of tectonic features of the Mid-Atlantic Ridge: 25–27°30' S, *J. Geophys. Res.* 96 (1991) 11741–11758.
- [22] H.J.B. Dick, W.B. Thompson, W.B. Bryan, Low angle faulting and steady-state emplacement of plutonic rocks at ridge-transform intersections, *Eos* (Trans. Am. Geophys. Union) 62 (1981) 406, abstract.
- [23] J.A. Karson, H.J.B. Dick, Tectonics of ridge-transform intersections at the Kane Fracture Zone, *Mar. Geophys. Res.* 6 (1983) 51–98.
- [24] P.R. Shaw, Ridge segmentation, faulting and crustal thickness in the Atlantic Ocean, *Nature* (London) 358 (1992) 490–493.
- [25] P.R. Shaw, J. Lin, Causes and consequences of variations in faulting style at the Mid-Atlantic Ridge, *J. Geophys. Res.* 98 (1993) 21839–21851.
- [26] C. Wolfe, G.M. Purdy, D.R. Toomey, S.C. Solomon, Microearthquake characteristics and crustal velocity structure at 29°N of the Mid-Atlantic Ridge: The architecture of a slow-spreading segment, *J. Geophys. Res.* 100 (1995) 24449–24472.
- [27] D.T. Sandwell, W.H.F. Smith, Gravity anomaly from Geosat

- and ERS1 satellite altimetry, *J. Geophys. Res.* (1997, in press).
- [28] G.M. Purdy, J.C. Sempéré, H. Schouten, D.L. Dubois, R. Goldsmith, Bathymetry of the Mid-Atlantic Ridge, 24°–31°N: A map series, *Mar. Geophys. Res.* 12 (1990) 247–252.
- [29] P.A. Rona, D.F. Gray, Structural behavior of fracture zones symmetric and asymmetric about a spreading axis: Mid-Atlantic Ridge (lat. 23°N to 27°N), *Geol. Soc. Am. Bull.* 91 (1980) 485–494.
- [30] H. Fujimoto, N. Seama, J. Lin, T. Matsumoto, T. Tanaka, K. Fujioka, Gravity anomalies of the Mid-Atlantic Ridge north of the Kane Transform fault, *Geophys. Res. Lett.* 23 (1996) 3431–3434.
- [31] E. Morris, R.S. Detrick, Three-dimensional analysis of gravity anomalies in the MARK area, Mid-Atlantic Ridge 23°N, *J. Geophys. Res.* 96 (1991) 4355–4366.
- [32] C. DeMets, R.G. Gordon, D.F. Argus, S. Stein, Current plate motions, *Geophys. J. Int.* 101 (1990) 425–478.
- [33] B.E. Tucholke, H. Schouten, Kane Fracture Zone, MAR, *Geophys. Res.* 10 (1988) 1–39.
- [34] H. Sloan, Ph. Patriat, Kinematics of the North American–African plate boundary between 28°N and 29°N during the last 10 Ma: evolution of the axial geometry and spreading rate and direction, *Earth Planet. Sci. Lett.* 113 (1992) 323–341.
- [35] R.L. Parker, The rapid calculation of potential anomalies, *Geophys. J.R. Astron. Soc.* 31 (1973) 447–455.
- [36] J. Phipps Morgan, D.W. Forsyth, Three-dimensional flow and temperature perturbations due to a transform offset: Effects on oceanic crustal and upper mantle structure, *J. Geophys. Res.* 93 (1988) 2955–2966.
- [37] J. Lin, J. Phipps Morgan, The spreading rate dependence of three-dimensional mid-ocean ridge gravity structure, *Geophys. Res. Lett.* 19 (1992) 13–15.
- [38] D.W. Sparks, E.M. Parmentier, The structure of three-dimensional convection beneath oceanic spreading centres, *Geophys. J. Int.* 112 (1993) 81–91.
- [39] R.L. Parker, S.P. Huestis, The inversion of magnetic anomalies in the presence of topography, *J. Geophys. Res.* 79 (1974) 1587–1593.
- [40] M. Tolstoy, A.J. Harding, J.A. Orcutt, Crustal thickness on the Mid-Atlantic ridge: Bull’s eye gravity anomalies and focused accretion, *Science* 262 (1993) 726–729.
- [41] T.A. Minshull, Along-axis variation in oceanic crustal density and their contribution to gravity anomalies, *Geophys. Res. Lett.* 23 (1996) 849–852.
- [42] W.H. Press, B.P. Flannery, S.A. Teukolsky, W.T. Vetterling, *Numerical Recipes — The Art of Scientific Computing*, Cambridge University Press, New York, NY, 1986.
- [43] D.W. Forsyth, Subsurface loading and estimates of the flexural rigidity of continental lithosphere, *J. Geophys. Res.* 90 (1985) 12623–12632.
- [44] A.D. Chave, D.J. Thomson, M.E. Ander, On the robust estimation of power spectra, coherences, and transfer functions, *J. Geophys. Res.* 92 (1987) 633–648.
- [45] F.J. Thomson, A.D. Chave, Jackknifed error estimates for spectral, coherences, and transfer functions, in: S. Kaykin (Ed.), *Advances in Spectrum Analysis and Array Processing*, vol. 1, Prentice-Hall, Englewood Cliffs, NJ, 1991, pp. 58–113.
- [46] E.M. Parmentier, W.F. Haxby, Thermal stress in the oceanic lithosphere: Evidence from geoid anomalies at fracture zones, *J. Geophys. Res.* 91 (1986) 793–7204.
- [47] M. McNutt, Lithospheric flexure and thermal anomalies, *J. Geophys. Res.* 89 (1984) 11180–11194.
- [48] J.A. Goff, B.E. Tucholke, J. Lin, G.E. Jaroslow, M.C. Kleinrock, Quantitative analysis of abyssal hills in the Atlantic Ocean: A correlation between axis crustal thickness and extensional faulting, *J. Geophys. Res.* 100 (1995) 22509–22522.
- [49] J. Phipps Morgan, E.M. Parmentier, Crenulated seafloor: Evidence for spreading-rate dependent structure of mantle upwelling and melting beneath mid-oceanic spreading center, *Earth Planet. Sci. Lett.* 129 (1995) 73–84.
- [50] P. Wessel, W.H.F. Smith, New version of the Generic Mapping tools released, *Eos (Trans. Am. Geophys. Union)* 76 (1995) 329.